MBoC | BRIEF REPORT

Myosin light chain kinase-driven myosin II turnover regulates actin cortex contractility during mitosis

Nilay Taneja, Sophie M. Baillargeon, and Dylan T. Burnette*
Cell and Developmental Biology, Vanderbilt University School of Medicine, Nashville, TN 37212

ABSTRACT **Force generation by the molecular motor myosin II (MII) at the actin cortex is a universal feature of animal cells. Despite its central role in driving cell shape changes, the mechanisms underlying MII regulation at the actin cortex remain incompletely understood. Here we show that myosin light chain kinase (MLCK) promotes MII turnover at the mitotic cortex. Inhibition of MLCK resulted in an alteration of the relative levels of phosphorylated regulatory light chain (RLC), with MLCK preferentially creating a short-lived pRLC species and Rho-associated kinase (ROCK) preferentially creating a stable ppRLC species during metaphase. Slower turnover of MII and altered RLC homeostasis on MLCK inhibition correlated with increased cortex tension, driving increased membrane bleb initiation and growth, but reduced bleb retraction during mitosis. Taken together, we show that ROCK and MLCK play distinct roles at the actin cortex during mitosis; ROCK activity is required for recruitment of MII to the cortex, while MLCK activity promotes MII turnover. Our findings support the growing evidence that MII turnover is an essential dynamic process influencing the mechanical output of the actin cortex.**

Monitoring Editor
Yu-li Wang
Carnegie Mellon University

Received: Sep 24, 2020
Revised: Jul 2, 2021
Accepted: Jul 19, 2021

INTRODUCTION

The actin cortex comprises a thin network of actin filaments underneath the plasma membrane of animal cells. Mechanical forces generated by the molecular motor myosin II (MII) at the actin cortex drive diverse processes such as cell division, cell migration, and tissue morphogenesis (Salbreux *et al*., 2012). While decades of studies have detailed the biochemical regulation of MII assembly and function in vitro (Sellers *et al*., 1982; Vicente-Manzanares *et al*., 2009), the dynamic regulation of MII function at the actin cortex in living cells has just begun to be elucidated. Rho-associated kinase (ROCK) and myosin light chain kinase (MLCK) are the two major kinases that activate MII by phosphorylation of its regulatory light chain (RLC) on Ser19 (pRLC), which facilitates assembly into bipolar filaments that can bind and contract actin filaments (Vicente-Manzanares *et al*., 2009). The RLC can then be further phosphorylated at Thr18 (ppRLC), which is thought to further increase MII contractility (Ikebe and Hartshorne, 1985; Mizutani *et al*., 2006).

Multiple studies have found distinct and overlapping functions for ROCK and MLCK during cell migration, cell survival, and cell division (Totsukawa *et al*., 2004; Connell and Helfman, 2006; Matsumura *et al*., 2011). During cell migration, MLCK regulates MII contractility at the leading edge, while ROCK regulates contractility at the cell rear (Katoh *et al*., 2001; Totsukawa *et al*., 2004). ROCK and MLCK inhibition have been shown to have opposing effects on cell survival in Ras-transformed MCF-10A cells; inhibition of MLCK, but not ROCK, results in increased cell death (Connell and Helfman, 2006). While ROCK and MLCK both activate MII contractility, whether the two kinases differentially regulate MII dynamics at the cortex remains less clear.

The actin cortex undergoes a series of dynamic, contractility-dependent rearrangements during cell division (Chugh and Paluch, 2018). On mitotic entry, the actin cortex assembles into an isotropic network of actin filaments and myosin-II motors (Bovellan *et al*., 2014; Chalut and Paluch, 2016). An increase in cortex tension driven by myosin-II contractility is required for cell rounding (Ramanathan *et al*., 2015; Toyoda *et al*., 2017). An inability to undergo cell rounding leads to cell division defects such as aberrant formation and

---

*Address correspondence to: Dylan T. Burnette (dylan.burnette@vanderbilt.edu).

Abbreviations used: FBS, fetal bovine serum; FRAP, fluorescence recovery after photobleaching; MII, motor myosin II; MLCK, myosin light chain kinase; RLC, regulatory light chain; ROCK, Rho-associated kinase; STR, short tandem repeat; TBST, Tris-buffered saline with Tween-20; WT, wild type.

positioning of the mitotic spindle, which can result in aneuploidy (Lancaster *et al.*, 2013; Bennabi *et al.*, 2020). Following cell rounding, the actomyosin network at the equatorial region assembles into a contractile ring, the constriction of which drives membrane deformation (Fujiwara and Pollard, 1976; Barr *et al.*, 2007). The cortex at the polar region remains isotropic and retains low myosin-II activity (Levayer and Lecuit, 2012; Bovellan *et al.*, 2014). Tight regulation of this low myosin-II activity at the polar regions is essential to maintain cell shape during cytokinesis (Guha *et al.*, 2005; Sedzinski *et al.*, 2011; Taneja *et al.*, 2020). The polar region is also characterized by membrane blebbing, which is thought to act as a intracellular pressure release valve during cytokinesis (Sedzinski *et al.*, 2011). However, increased polar cortex tension results in shape instabilities in the form of large membrane blebs and is associated with increased chromosome missegregation and cytokinetic failure (Sedzinski *et al.*, 2011; Taneja *et al.*, 2020). This has led to the idea that bleb size beyond a critical threshold increases the propensity of cell shape instabilities (Sedzinski *et al.*, 2011). On the other hand, the generation and retraction of large blebs is utilized in multiple cell types to drive cell migration (Charras and Paluch, 2008). Despite their critical roles in cytokinesis and cell migration, the regulatory mechanisms that control bleb nucleation, growth, and retraction remain poorly understood.

Tension generation by the actin cortex is an active process and is driven by dynamic behaviors such as assembly and turnover of its components. It is intuitive that assembly of contractile system components would be required for tension generation. However, it is increasingly appreciated that the disassembly of components that drive turnover of the actin cortex is an equally important process in driving membrane deformations under tension. Coordinated turnover of myosin-II, actin filaments, and actin cross-linkers is required for bleb retraction (Fritzsche *et al.*, 2016; Taneja and Burnette, 2019). Similarly, turnover of contractile ring components is essential for cleavage furrow ingression (Murthy and Wadsworth, 2005; Chew *et al.*, 2017). The mechanisms that regulate myosin-II disassembly and its effects on actin cortex mechanics are not well understood.

In this study, we investigate the regulatory mechanisms underlying myosin-II turnover at the mitotic cell cortex. The metaphase cortex is an ideal model system for these studies, as it is isotropic, devoid of cell shape fluctuations, and amenable to direct biophysical measurements. While a role for ROCK in mitosis is well established (Chircop, 2014), the role of MLCK remains less clear. MLCK is dispensable for early mammalian embryonic divisions since knockout of MLCK is not embryonic lethal but results in neonatal lethality (Somlyo *et al.*, 2004). In cultured cells, expression of the N-terminal region of MLCK causes multinucleation and spindle assembly defects (Dulyaninova and Bresnick, 2004). Inhibition of MLCK in multiple cancer lines also causes multinucleation and cytokinesis defects (Wu *et al.*, 2010). However, the mechanism by which MLCK exerts its varied effects remains unknown (Matsumura *et al.*, 2011). This could in part be attributed to a lack of understanding of the role of MLCK at the actin cortex. We found that MLCK inhibition unexpectedly resulted in lower MII turnover and higher cortical enrichment, which correlated with alteration of the balance between mono- and diphosphorylated RLC. Using direct biophysical measurements, we found, paradoxically, that inhibition of MLCK resulted in increased cortex tension. Increased cortex tension, coupled with lower turnover, also correlated with increased membrane bleb nucleation and slower bleb retraction.

RESULTS AND DISCUSSION

During interphase, MLCK and ROCK drive spatially restricted preferential RLC phosphorylation, with MLCK creating pRLC but not ppRLC (Kassianidou *et al.*, 2017). MLCK and ROCK act on two different actin networks: peripheral stress fibers and central stress fibers, respectively (Beach *et al.*, 2017; Kassianidou *et al.*, 2017). To test how MLCK regulates RLC phosphorylation during metaphase—where the cortex is organized as a single isotropic network—we localized endogenous pRLC and ppRLC. We found uniform localizations of pRLC and ppRLC around the cortex (Figure 1A). To disrupt MLCK activity, we used the small molecule inhibitor ML-7. We found that MLCK inhibition resulted in a decrease in pRLC but no significant difference in the localization of ppRLC (Figure 1, A–C). We confirmed these results using two additional methods of MLCK inhibition (Figure 1, A–C): we used siRNA-mediated MLCK depletion or kinase dead MLCK overexpression (OE), which has been previously shown to mimic MLCK inhibition (Dulyaninova *et al.*, 2004) (Figure 1B). These data show that MLCK inhibition results in a decrease in pRLC, but not ppRLC localization. In contrast, we found that ROCK inhibition resulted in a significant loss of ppRLC from the cortex during metaphase, which is consistent with what has been previously shown during cytokinesis (Kondo *et al.*, 2013) (Supplemental Figure S1A).

We hypothesized that the reduction in pRLC after MLCK inhibition would be correlated with a reduction in MIIA heavy chain at the metaphase cortex. Surprisingly, we found that MLCK inhibition resulted in an increase in MII heavy chain enrichment, despite a decrease in pRLC (Figure 1, D and E). We confirmed the increase in enrichment of MIIA using two additional methods of MLCK inhibition (Figure 1, D and E). These data suggest that the phosphorylation state of RLC can influence the behavior of the heavy chain at the cortex.

We reasoned that the increased enrichment of MII at the cortex could result from slower cortical turnover, which would result in a higher steady-state cortical population of MII. A role for phosphorylation in regulating turnover of the RLC has been previously found in *Drosophila* embryos as well as cultured cells in interphase (Watanabe *et al.*, 2007; Kasza *et al.*, 2014). Since MLCK inhibition alters the relative localization of pRLC versus ppRLC, we wondered whether this could underlie the observed changes in turnover of the heavy chain during mitosis. We first measured the turnover of wild-type RLC (WT RLC) using fluorescence recovery after photobleaching (FRAP) at the metaphase cortex (Figure 2, A–C). To test if the phosphorylation status of the RLC regulates turnover during mitosis, we employed phospho-mimetic and phospho-null mutants developed previously (Watanabe *et al.*, 2007; Beach *et al.*, 2011). We found that mutating both Thr18 and Ser19 to aspartate (DD-RLC)—mimicking ppRLC—resulted in a ~2-fold increase in the half-life of the RLC (Figure 2, B and C). This was accompanied by increased cortical enrichment of the RLC (Figure 2A). Conversely, mutating both Thr18 and Ser19 to alanine (AA-MLC)—mimicking unphosphorylated RLC—resulted in a significant decrease in half-life as well as a marked reduction in cortical enrichment (Figure 2, A–C). To test the effect of only Ser19 phosphorylation on RLC turnover, we created a T18AS19D mutant, which cannot be phosphorylated at the Thr18 site and acts as a phospho-mimetic at the Ser19 site (AD-RLC). We found that the AD-RLC mutant turned over at rates intermediate between the WT and the DD mutant (Figure 2, A–C).

Given the increased enrichment of MIIA heavy chain on MLCK inhibition and the slower turnover of DD-RLC, we predicted MLCK inhibition would result in slower heavy chain turnover. We found that the MIIA heavy chain recovered with a half-life of ~9.8 s, which was comparable to the turnover rate of RLC (Figure 2, C–E), as well as consistent with our previous report (Taneja and Burnette, 2019). We found that treatment with ML-7, kinase-dead MLCK OE, or knockdown of MLCK each caused an increase in the half-life of MIIA at the

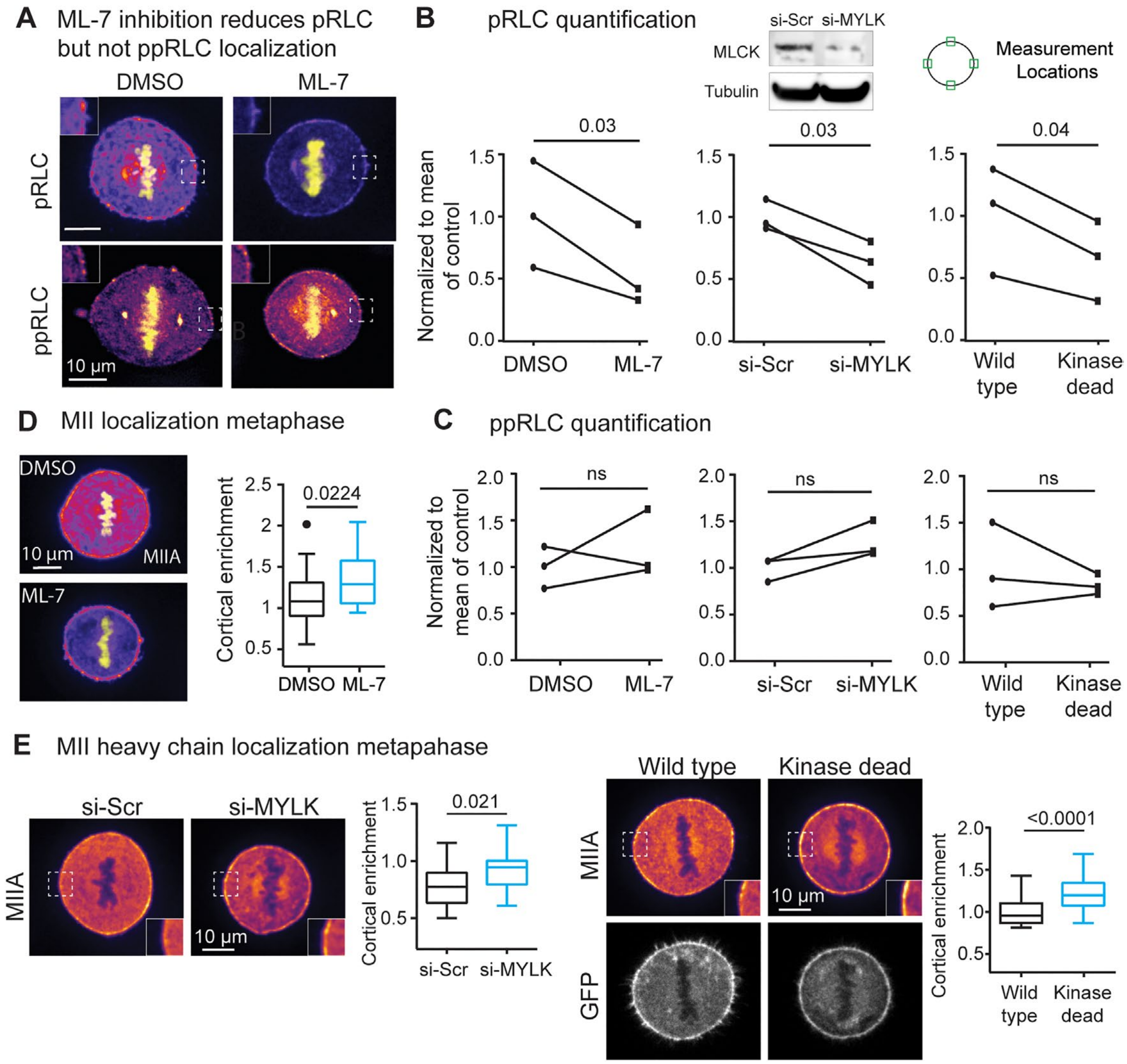

FIGURE 1: Effect of MLCK inhibition on MII heavy and light chain localization. (A) Endogenous pRLC and ppRLC during metaphase (mpl-Inferno LUT). Insets: enlarged view of cortex. (B) pRLC quantification; *n* = 26 DMSO treated, 23 ML-7 treated, 31 WT MLCK OE, 28 kinase dead MLCK OE, 27 si-Scr, and 19 si-MYLK cells; *N* = 3 experiments. Inset: knockdown validation using Western blot. (C) ppRLC quantification; *n* = 24 DMSO, 25 ML-7 treated, 24 si-Scr, 19 si-MYLK, 20 WT MLCK OE, and 20 kinase dead MLCK OE cells; *N* = 3 experiments. (D) Endogenous MIIA heavy chain during metaphase (mpl-Inferno LUT). Cortical enrichment of MIIA at the metaphase cortex, *n* = 24 DMSO and 26 ML-7 treated cells; *N* = 3 experiments. (E) MIIA cortical enrichment at the metaphase cortex on MLCK inhibition. Insets: enlarged view of cortex. *n* = 20 si-Scr treated, 18 si-MYLK treated, 30 WT MLCK OE, and 36 kinase dead MLCK OE cells; *N* = 3 experiments.

cortex (Figure 2, D and E). Taken together, our data show that MLCK inhibition is correlated with increased relative abundance of the diphosphorylated—more contractile—species of the RLC, as well as increased residence time of MII at the cortex. To test if these changes affected the physical properties of the cortex, we performed direct measurements of cortex tension using micropipette aspiration (Tinevez *et al.*, 2009; Taneja *et al.*, 2020). We hypothesized that the stabilization of highly contractile MII motors should result in increased cortex tension. Indeed, we found that MLCK inhibition using either ML-7 treatment or knockdown of MLCK resulted in an increase in cortex tension during metaphase (Figure 2, F and G). We next wanted to test how these changes in myosin-II turnover and tension generation affect actin cortex assembly and function. One of the few model systems amenable to studying cortex assembly is the bleb membrane (Charras *et al.*, 2006). Membrane blebs are proposed to be nucleated on local cortex rupture at high cortex tensions (Paluch *et al.*, 2005). After bleb nucleation, a new actin cortex is assembled on the bleb membrane, which then drives retraction and reintegration of the bleb into the cell cortex (Charras *et al.*, 2008).

Focused laser-mediated cortex damage, which mimics spontaneous bleb formation by cortex rupture, can be used to test both bleb growth and bleb retraction (Tinevez *et al.*, 2009; Taneja and Burnette, 2019; Taneja *et al.*, 2020). The size of the initial bleb is dependent on cortex tension and intracellular pressure, while the rate of bleb retraction is dependent on MII turnover (Charras *et al.*, 2008; Tinevez *et al.*, 2009; Taneja and Burnette, 2019). In control metaphase cells, cortex ablation resulted in the generation of a bleb that subsequently retracted (Figure 3, A and B). As a control, we inhibited ROCK, which reduces cortex tension (Tinevez *et al.*, 2009). ROCK inhibition resulted in an absence of blebs on cortex ablation (Figure 3, A and B). Interestingly, MLCK inhibition using either

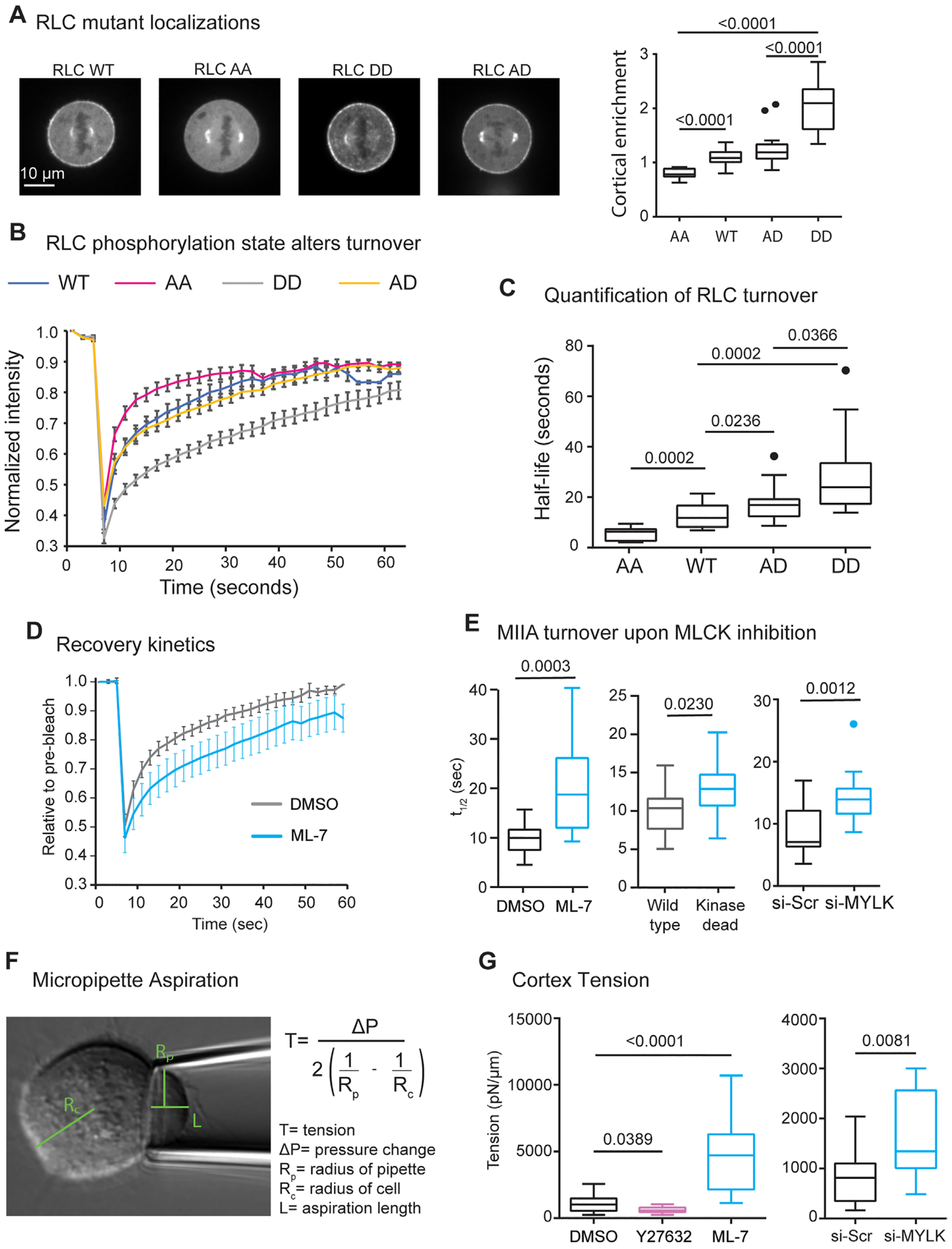

$$T = \frac{\Delta P}{2\left(\frac{1}{R_p} - \frac{1}{R_c}\right)}$$

T= tension
ΔP= pressure change
R_p= radius of pipette
R_c= radius of cell
L= aspiration length

FIGURE 2: MLCK inhibition reduces MII turnover during mitosis. (A) Cortical localization of MII RLC mutants; *n* = 13 AA, 13 WT, 17 AD, 15 DD RLC cells; *N* = 3 experiments. (B) Averaged FRAP curves showing recovery kinetics of MII RLC mutants. (C) Half-life of MLC-WT, AA, DD, and AD mutants; *n* = 11 MLC-AA,12 MLC-WT,15 MLC-AD, and 13 MLC-DD expressing cells; *N* = 3 experiments; *p* values are stated in graphs. (D) Averaged FRAP recovery kinetics for MIIA heavy chain during metaphase. (E) Half-life of MIIA heavy chain at the metaphase cortex on ML-7 treatment, siRNA-mediated knockdown or OE of kinase dead MLCK. *n* = 15 DMSO treated, 13 ML-7 treated, 19 WT MLCK OE, 21 kinase dead MLCK OE, 15 si-Scr, and 15 si-MYLK cells; *N* = 3 experiments. (F) Representative image of micropipette aspiration during metaphase. (G) Cortex tension on ROCK and MLCK inhibition; *n* = 19 DMSO, 12 Y27632, 20 ML-7, 15 si-Scr, and 16 si-MYLK cells; *N* = 3 experiments.

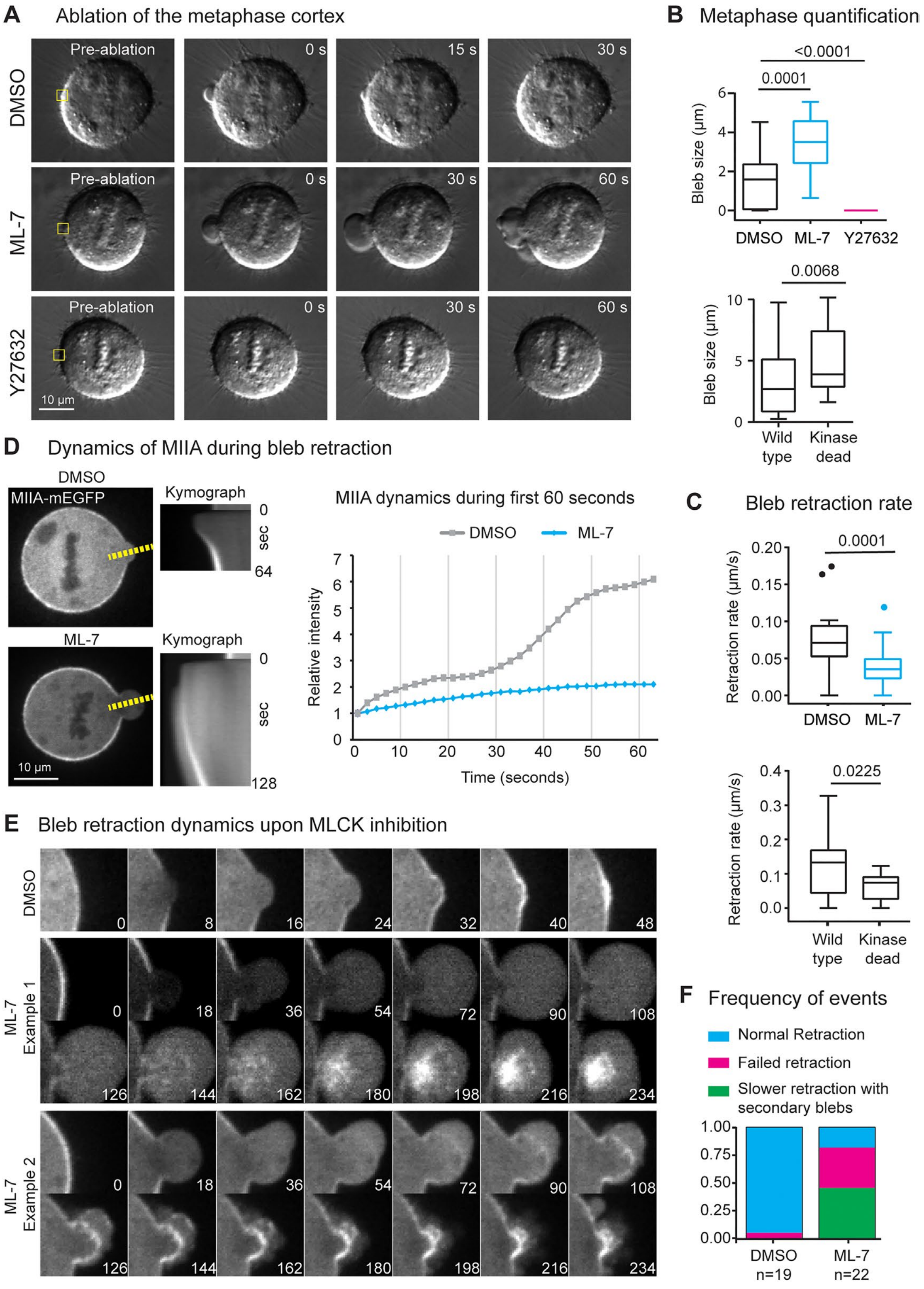

FIGURE 3: MLCK inhibition alters bleb growth and retraction. (A) Focused laser-mediated cortical damage during metaphase. Yellow box denotes ROI used for damage. (B) Bleb size following cortical damage; *n* = 28 DMSO treated, 25 ML-7 treated, 13 Y27632 treated, 23 WT MLCK OE, and 24 kinase dead MLCK OE cells; *N* = 3 experiments. (C) Bleb retraction rate from DIC data following cortical damage; *n* = 21 DMSO treated, 25 ML-7 treated, 14 WT MLCK OE, and 22 kinase dead MLCK OE cells; *N* = 3 experiments. (D) Cortical dynamics of MIIA-mEGFP on focused laser-mediated cortical damage. Dotted yellow line was used to create kymograph. Inset: representative intensity profile created using the kymograph comparing the dynamics of MIIA at the bleb membrane; 0 s denotes the time point immediately following cortical damage. (E) MIIA dynamics at the bleb membrane following cortical damage. (F) Relative occurrence of bleb retraction outcomes- normal (as in DMSO montage in E), failed retraction (as in ML-7 Example 1 in E) and slower retraction with secondary blebs as in ML-7 Example 2).

treatment with ML-7 or kinase-dead MLCK OE resulted in a significant increase in the size of the bleb created immediately following ablation (Figure 3, A and B). However, unlike control cells, we observed that the overall rate of bleb retraction was significantly reduced (Figure 3, A–C). We also noted the initiation of secondary blebs on retracting primary blebs (Figure 3A).

MIIA recruitment to the bleb cortex is required for bleb retraction (Charras *et al.*, 2006; Taneja and Burnette, 2019). To test whether MLCK inhibition perturbed the recruitment of MIIA to the newly formed bleb cortex, we assessed the dynamics of MIIA at the cortex after ablation. In control cells, we found MIIA showed stereotypical enrichment at the bleb membrane (Figure 3, D and E). On MLCK inhibition, we found MIIA showed delayed recruitment to the bleb membrane (Figure 3, D and E). In ~36% of blebs, MIIA remained localized as distinct foci and appeared to flow back toward the cortex, while the bleb membrane did not retract (Figure 3, E and F, Example 1). We speculate this could result from defects in membrane-cortex attachment. Additionally, in ~45% of blebs, we observed the formation of secondary blebs (Figure 3, E and F, Example 2). We speculate this may be driven by the inability of MII to turn over and thus not allow cortex rearrangement during bleb retraction. Taken together, our data show that inhibition of MLCK causes increased bleb initiation but slows down bleb retraction.

Previous work has shown that increased cortex tension drives bleb formation at the polar cortex during cytokinesis (Sedzinski *et al.*, 2011; Taneja *et al.*, 2020). Given that MLCK inhibition increased cortex tension, we hypothesized that MLCK inhibition should also increase spontaneous bleb formation during cytokinesis. Indeed, MLCK inhibition using either ML-7 treatment or siRNA knockdown caused a significant increase in the number of blebs while the mean bleb size remained unchanged (Figure 4, A–C). Delayed bleb retraction and initiation of secondary blebs were also observed during spontaneous bleb formation in cells undergoing cytokinesis (Supplemental Movie S1). As a control, we found ROCK inhibition resulted in a complete cessation of membrane blebbing, consistent with previous reports (Figure 4A) (Tinevez *et al.*, 2009).

To test whether changes in blebbing correlated with changes in MII heavy and light chain recruitment at the polar cortex, we localized MIIA heavy chain, pRLC and ppRLC, during cytokinesis. MLCK inhibition increased the localization and enrichment of MIIA at the polar cortex, while localization at the equatorial cortex was not altered (Figure 4, D and F; Supplemental Figure S1B). Consistent with our measurements at the metaphase cortex, MLCK inhibition resulted in a significant decrease in pRLC localization, but not ppRLC localization at the polar cortex (Figure 4G). On the other hand, both pRLC and ppRLC localization were decreased at the equatorial cortex (Supplemental Figure S1C). As a control, we found ROCK inhibition caused a global reduction in pRLC, ppRLC, and MIIA localization at the cortex during cytokinesis, in agreement with previous reports (Supplemental Figure S1D) (Kosako *et al.*, 2000; Dean *et al.*, 2005; Watanabe *et al.*, 2007; Kondo *et al.*, 2013). Taken together, our data suggest that ROCK is involved in MII recruitment, while MLCK is involved in MII turnover at the cortex.

To test whether the increase in membrane blebbing was also observed during interphase, we turned to filamin-deficient M2 cells that constitutively bleb during interphase (Charras *et al.*, 2006). ROCK inhibition caused a complete cessation in blebbing, in agreement with previous reports (Bergert *et al.*, 2012) (Figure 4, H and I). On the other hand, MLCK inhibition caused a significant increase in the proportion of blebbing M2 cells, in line with our observations during mitosis (Figure 4, H and I). We also evaluated overall cell survival on MLCK and ROCK inhibition. Consistent with previous reports (Connell and Helfman, 2006), we found inhibition of MLCK using either ML-7 or siRNA knockdown also reduced cell proliferation assessed from increase in confluence using automated imaging and analysis (Supplemental Figure S2). ROCK inhibition, on the other hand, had no effect on cell proliferation and attenuated the effects of MLCK inhibition when added simultaneously (Supplemental Figure S2).

Most studies investigating the cellular role of MII contractility focus on how MII assembles into filaments and localizes to different cellular compartments to perform different functions. There is mounting evidence that regulated disassembly of contractile structures is equally important to drive cell shape changes. For instance, actin turnover has been shown to be essential in contractile ring constriction from yeast to mammalian cells (Murthy and Wadsworth, 2005; Chew *et al.*, 2017). In this study, we show that MLCK plays an unexpected role in regulating MII dynamics at the actin cortex during mitosis. Specifically, we found that MLCK inhibition resulted in slower MII turnover. These changes correlated with changes in RLC homeostasis, with MLCK inhibition reducing pRLC, but not ppRLC, at the cortex. We further found that DD-RLC shows significantly lower turnover compared with AD-RLC. This suggests that the monophosphorylated species of RLC generates a rapidly turning over population of MII, while the diphosphorylated species of RLC generates stable contractile MII motors. On inhibition of MLCK, the proportion of rapidly turning over pRLC associated motors is reduced, increasing the relative proportion of stable ppRLC-associated motors.

In agreement with these results, we further found that cortex tension significantly increased on MLCK inhibition. This increase in cortex tension correlated with increased bleb formation and growth. Interestingly, a previous study found that injection of the catalytic fragment of MLCK resulted in higher polar blebbing (Fishkind *et al.*, 1991). This suggests that MLCK activity must be finely tuned to maintain homeostatic contractility of MII since both inhibition and hyper-activation result in cortex instability. On the other hand, we found bleb retraction on MLCK inhibition was significantly altered, resulting in either complete failure or slower retraction. This uncoupling of bleb initiation and bleb retraction shows that in assessing MII function, it is important to measure localization of both the phosphorylated RLC species and the turnover rate of the heavy chain. The monophosphorylation-mediated rapid turnover of MII may be required for generating contractility in structures that undergo rapid changes in shape (e.g., bleb retraction). In support of this idea, MLCK phosphorylates RLC at the dynamic leading edge of migrating cells, while ROCK phosphorylates RLC in stable stress fibers in the middle or rear of the cell (Totsukawa *et al.*, 2004).

During cytokinesis, we found that MLCK inhibition had distinct effects on the polar and equatorial cortex, where MLCK inhibition altered pRLC homeostasis and MIIA cortical localization only at the polar cortex. This observation was also noted previously in dividing sea urchin eggs (Uehara *et al.*, 2008). In this work, the authors speculated that this increase in MII localization at the polar cortex could result from "physical stresses." Our results mechanistically link these observations to the role of MLCK in RLC homeostasis and heavy chain turnover. In support of our model, it has been previously reported that the turnover of MII is faster at the polar cortex compared with the equatorial cortex (Srivastava and Robinson, 2015). Our findings therefore suggest that distinct mechanisms regulate MII dynamics at the equatorial versus polar cortex.

In further agreement with this idea, we observed that both MLCK and ROCK inhibition reduced the rate of furrow ingression (Supplemental Figure S1, F and G), with MLCK inhibition showing a weaker effect, which is consistent with previous reports (Kosako *et al.*, 2000;

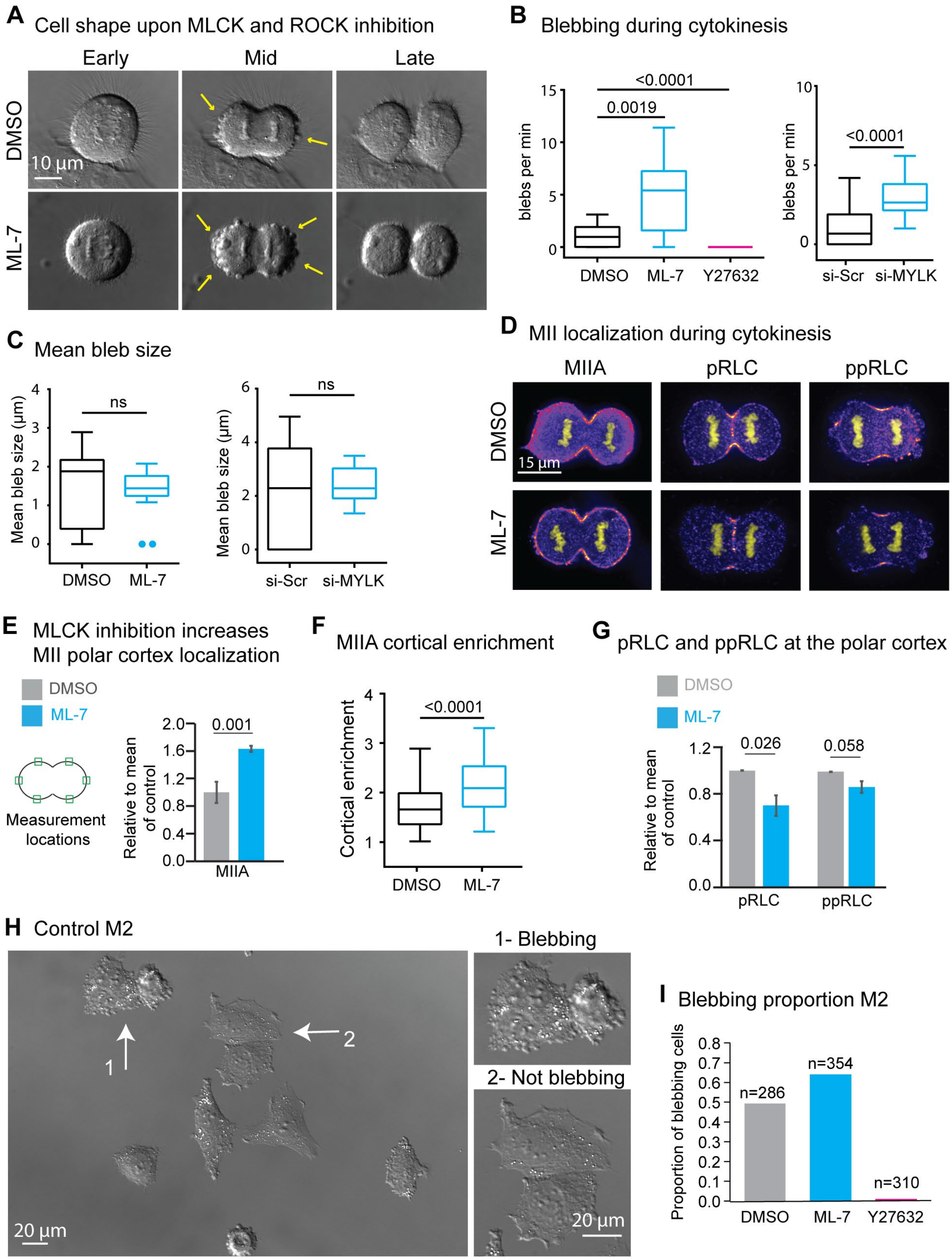

FIGURE 4: Inhibition of MLCK reduces MII turnover and RLC homeostasis at the polar cortex during cytokinesis. (A) Cytokinesis on treatment with DMSO, ML-7 or Y27632. Yellow arrows: blebs. (B, C) Number of blebs per minute (B) and mean bleb size (C) in DMSO, ML-7, Y27632, si-Scr and si-MYLK cells. *n* = 16 DMSO, 15 ML-7, 14 Y27632, 18 si-Scr and 18 si-MYLK treated cells; *N* = 3 experiments. (D) Localization of MIIA, pRLC and ppRLC during cytokinesis. (E) MIIA polar cortex localization quantification. *n* = 17 DMSO and 14 ML-7 treated cells; *N* = 3 independent experiments. (F) Cortical enrichment of MIIA heavy chain at the polar cortex. *n* = 42 DMSO and 52 ML-7 treated cells; *N* = 3 experiments. The values were normalized to the mean of the control. (G) pRLC and ppRLC localization at the polar cortex. pRLC: *n* = 28 DMSO and 26 ML-7 treated cells; *N* = 3 experiments. ppRLC: *n* = 35 DMSO and 32 ML-7 treated cells; *N* = 3 experiments. (H) Control M2 melanoma cells 5 h post plating. Insets: enlarged views of blebbing (1) and not blebbing (2) cells. (I) Proportion of blebbing M2 cells on DMSO, ML-7 and Y27632 treatment; *N* = 3 experiments.

Hickson *et al.*, 2006; Maddox *et al.*, 2007). These differences could likely result from the distinct actin cortex architectures reported in these two networks, with the equatorial cortex containing ordered, bundled actin filaments and the polar cortex containing a more isotropic network (Bovellan *et al.*, 2014). Indeed, recent studies have shown that actin architecture can regulate cortex tension generation independently of MII activity (Chugh *et al.*, 2017; Weirich *et al.*, 2021). In addition, the differential dynamics of ROCK and MLCK at the two networks may also contribute to these differences. It would also be interesting to investigate the relative contribution of these kinases in different cell types and across development, since some cell types such as Rat1A cells and sea urchin embryos do not require ROCK activity and solely depend on MLCK activity to drive furrow ingression (Yoshizaki *et al.*, 2004; Uehara *et al.*, 2008). Utilizing sensitive biosensors of ROCK and MLCK would be required to determine the mechanisms controlling the spatial activities of these two kinases during cytokinesis. Future studies are also likely to reveal additional regulatory proteins that impinge on MII turnover and function and how these different regulators are spatially organized and controlled at the nanoscale in the actin cortex.

MATERIALS AND METHODS

Request a protocol through *Bio-protocol*.

Cell lines, growth conditions, and reagents

HeLa (ATCC, CCL-2) cells were cultured in growth media comprised of DMEM (Mediatech, Inc., Manassas, VA, #10-013-CV) containing 4.5 g/L L-glutamine, L-glucose, and sodium pyruvate and supplemented with 10% fetal bovine serum (FBS; Sigma-Aldrich, St. Louis, MO, #F2442). M2 melanoma cells were cultured in minimal essential medium supplemented with Earle's salts, 10 mM HEPES, and 10% FBS. Growth substrates were prepared by coating #1.5 glass coverslips (In Vitro Scientific, #D35C4-20-1.5N or #D35-20-1.5N) with 10 μg/ml FN (Corning, Corning, NY, #354008) in PBS (Mediatech, Inc., #46-013-CM) at 37°C for 1 h.

For protein expression, cells were transiently transfected using Fugene 6 (Promega, Madison, WI, #E2691) as per the manufacturer's instructions overnight in a 25-cm^2 cell culture flask (Genessee Scientific Corporation, San Diego, CA, #25-207) before plating on a growth substrate.

For pharmacological treatments, cells were cultured on the growth substrate for 24 h prior to treatment. Y27632 (Sigma, #Y0503) and ML-7 (Sigma, #I2764) were used at a concentration of 10 μM. DMSO was used at a concentration of 1:1000. ML-7 dilution was performed in DMEM supplemented with 5% FBS. Control cells treated with DMSO diluted in DMEM supplemented with 5% FBS were indistinguishable from cells treated with DMSO diluted in 10% FBS.

Alexa Fluor-488 phalloidin (#A12379), Alexa Fluor-568 phalloidin (#A12380), and Alexa Fluor 488-goat anti-rabbit (#A11034) were purchased from Life Technologies (Grand Island, NY). Rabbit anti-myosin IIA (#909801) was purchased from BioLegend (San Diego, CA). Rabbit anti-myosin IIB (#3404S), anti-RLC (pS19) (3671S), and anti-RLC (pT18S19) (3674S) were purchased from Cell Signaling Technology (Danvers, MA). Rabbit anti-MLCK (ab76092) was purchased from Abcam (Cambridge, MA). Mouse anti-tubulin (DM1α) was purchased from Sigma (T6199).

Cell line authentication

The HeLa cell line used in this study was a gift from D.A. Weitz (Harvard University), and the M2 melanoma cells were a gift from Matthew Tyska. These lines were authenticated by Promega and ATCC using their "Cell Line Authentication Service" in 2015 and 2019, respectively. The methods and test results received from Promega and ATCC are as follows:

"Methodology: 17 short tandem repeat (STR) loci plus the gender determining locus, Amelogenin, were amplified using the commercially available PowerPlex 18D Kit from Promega. The cell line sample was processed using the ABI Prism 3500xl Genetic Analyzer. Data were analyzed using GeneMapper ID-X v1.2 software (Applied Biosystems). Appropriate positive and negative controls were run and confirmed for each sample submitted.

"Data Interpretation: Cell lines were authenticated using STR analysis as described in 2012 in ANSI Standard (ASN-0002) Authentication of Human Cell Lines: Standardization of STR Profiling by the ATCC Standards Development Organization (SDO)"

HeLa- CCL-2 results- "Test Results: The submitted profile is an exact match for the following ATCC human cell line(s) in the ATCC STR database (eight core loci plus Amelogenin): CCL-2 (HeLa)."

M2 results- "Test Results: Submitted sample, STRA12409 (M2 melanoma), is an exact match to ATCC cell line CRL-2500 (A7). When compared with the reference profile the submitted profile shows and extra #10 allele at the TPOX locus. The cell line, (M2), has been discontinued by ATCC."

Mycoplasma monitoring. All cell lines were checked for potential mycoplasma infection using DAPI throughout the course of this study.

Plasmids

MIIA mEmerald (Addgene, Cambridge, MA, #54190), MIIA mApple (Addgene, #54929), and MIIB mEmerald (Addgene, #54192) were gifts from Michael Davidson. WT MLCK mEGFP (Addgene #46316) and kinase dead MLCK mEGFP (Addgene #46317) were gifts from Anne Bresnick. MIIA mEGFP (Addgene, #11347) was a gift from Robert Adelstein. MIIB mEGFP (Addgene, #35691) was a gift from Venkaiah Betapudi. MRLC-WT mEGFP (Addgene #35680), MRLC-AA mEGFP (Addgene #35681), and MRLC-DD (Addgene #35682) mEGFP were gifts from Thomas Egelhoff. MRLC-AD mEGFP was created by mutagenesis of the MRLC-WT template using a modified site-directed PCR mutagenesis method (Liu and Naismith, 2008) that we have described previously (Taneja and Burnette, 2019; Taneja *et al.*, 2020). The primers used for the mutagenesis were the following: Forward primer: 5′-cgggccgcagacaatgtcttcgcaatgtttgaccagtccc-3′ and Reverse primer: 5′-attgtctgcggcccgctgtggccgcttcttggtgg-3′.

Phase and DIC imaging

Phase and DIC imaging was performed on a Nikon (Melville, NY) Eclipse Ti-E inverted microscope equipped with a Nikon 1.45 NA 100× oil DIC, 0.95 NA 40× Air DIC, and a 0.4 NA 20× Air Phase objective. Samples were maintained at 37°C with 5% CO_2 using a Tokai Hit Stage Incubator (Shizuoka-ken, Japan). For quantifying cell proliferation, imaging was performed on an Incucyte S3 (4647, Essen BioScience) microscope equipped with a 20× objective and maintained in a tissue culture incubator at 37°C and 5% CO_2.

Fluorescence imaging, cortical ablation, and FRAP

FRAP and cortical ablation were performed on a Nikon Eclipse Ti-E inverted microscope equipped with a Yokogawa CSU-X1 spinning disk head, 1.4 NA 60× oil objective, Andor DU-897 EMCCD, and a dedicated 100 mW 405 diode ablation laser, generously provided by the Nikon Center of Excellence at Vanderbilt University. The instrument was controlled using Nikon Elements AR software. For ablation, a 1.4 µm × 1.4 µm ROI was used for all experiments. A DIC and/or fluorescence image was acquired before ablation, followed by ablation using a miniscanner. A pixel dwell time of 500 µs, 50% laser power was used for a duration of 1 s, followed by acquiring DIC or fluorescence images at 2-s intervals. Samples were maintained at 37°C with 5% CO_2 using Tokai Hit Stage Incubator. To localize endogenous MII heavy and light chain in fixed HeLa cells, single slices through the middle of the cell were acquired at 60× magnification using spinning disk microscopy or widefield microscopy. To appropriately compare the intensity, paired controls were always stained in parallel and imaged using the same imaging parameters. All data points within a biological replicate were normalized to the mean signal of the control data set from that biological replicate.

Knockdown experiments

Accell siRNA against the 3′-UTR of MYLK (A-005351-27-0005, target sequence CUAGCAGCUUCAGACAUUU) was purchased from GE Dharmacon. Knockdown experiments were performed in 24-well plates using Lipofectamine 2000 (Life Technologies, #1690146) as per instructions provided by the manufacturer. Knockdown was performed for 72 h, after which cells were either plated on the growth substrate for imaging or lysed for Western blot experiments. We achieved a 60 ± 8% reduction in protein levels (Figure 1B, $N = 4$ independent experiments).

Western blotting

Gel samples were prepared by mixing cell lysates with LDS sample buffer (Life Technologies, #NP0007) and sample reducing buffer (Life Technologies, #NP00009) and boiled at 95°C for 5 min. Samples were resolved on Bolt 4–12% gradient Bis-Tris gels (Life Technologies, #NW04120BOX). Protein bands were blotted onto a nylon membrane (Millipore). Blots were blocked using 5% NFDM (Research Products International Corp, Mt. Prospect, IL, #33368) in Tris-buffered saline with Tween-20 (TBST). Antibody incubations were also performed in 5% NFDM in TBST. Blots were developed using the Immobilon Chemiluminescence Kit (Millipore, #WBKLS0500).

Micropipette aspiration

Micropipette aspiration was performed as reported previously (Taneja *et al.*, 2020). Briefly, microneedles (World Precision Instruments, 0.75 mm inner diameter and 1.0 mm outer diameter) were pulled to a centimeter-long taper using a Narishige PC-100 needle puller. Needles were cut to a diameter ranging between 10 and 15 µm and fire-polished using a Narishige MF-900 microforge.

To perform micropipette aspiration, the needles were mounted on an Eppendorf Transfer Man 4R micromanipulator that was magnetically attached to the optical table. Cells were visualized using DIC (Plan Apo 0.95 NA, 40× Nikon DIC air objective, with 1.5× optical zoom on a Nikon Eclipse Ti inverted microscope controlled using Elements software). Cells were maintained at 37°C with 5% CO_2 using a Tokai Hit stage incubator. Metaphase cells were identified using the appearance of a tight metaphase plate using DIC. The needle was then positioned close to the cell until the pipette made firm contact with the cell. Automated pressure control was performed using Fluigent's Microfluidic Automation Tool. For our experiments, we started at a pressure of zero and increased the negative (suction) pressure at a rate of 0.02 mbar per second. To complete the experiment and release the cell from the micropipette needle, the imaging program and pressure protocol were stopped when the cell was sufficiently aspirated. Cortex tension was then calculated by analyzing the DIC time montages as reported previously (Taneja *et al.*, 2020).

Data quantification

To quantify the rate of cleavage furrow ingression, we created kymographs from DIC time montages acquired at 30-s intervals, as described previously (Taneja *et al.*, 2020). Ingression rate was measured as the displacement of one side of cleavage furrow in µm per unit time. Ingression rates were normalized to the mean of the control condition. Polar blebbing was quantified as the total number of blebs nucleated per unit time as described previously (Taneja *et al.*, 2020). Briefly, DIC time montages acquired at 30-s intervals were used for the analysis. Every in-focus bleb was measured between the times immediately following the end of Anaphase A (sister chromatids no longer move away from each other; this was also verified by making a kymograph across the long axis of the cytokinetic cell) and the end of cleavage furrow ingression. The total number of blebs was then normalized to the number of min for which the analysis was performed. For quantifying focused laser-mediated cortical damage data, DIC images were acquired at 2-s intervals following cortical damage. The size of the bleb (long axis) was measured at the first frame following ablation. A kymograph was created using a 3-pixel wide line placed parallel to the direction of bleb retraction. The rate of bleb retraction was calculated as the distance travelled by the bleb membrane per unit time.

Analysis of turnover of MII heavy and light chains was performed as done previously (Taneja and Burnette, 2019). Briefly, confocal time montages acquired at 2-s intervals were first aligned using the StackReg plug-in in Fiji. Three ROIs were then drawn at 1) a bleached region, 2) an unbleached region, and 3) background. Mean intensity over time was calculated for each of the three ROIs using the Multi Measure function in the ROI manager. Analysis and curve fitting were performed using the easyFRAP algorithm in MATLAB (Rapsomaniki *et al.*, 2015). Double normalization was performed to account for background correction and photobleaching, followed by fitting the normalized curves to a second-degree exponential to obtain the half-maximal recovery time (see Rapsomaniki *et al.*, 2015, for details on fitting equations and normalization). Curves with poor fits (with $R^2 < 0.9$) were not included for analysis. Averaged FRAP curves were created in Excel, and Tukey plots to compare half-life were created in GraphPad.

Analysis of endogenous localization of MII heavy and light chains was performed as previously described (Taneja *et al.*, 2020). Briefly, ROIs were arbitrarily placed as shown in Supplemental Figure S2 and mean cortical intensity was measured. The background subtraction was performed by measuring background fluorescence using a similar size ROI. For calculating enrichment of the heavy chain, the average cortical signal was divided by the cytoplasmic signal. For calculating absolute levels of pRLC or ppRLC, the mean cortical intensity normalized to the paired control was compared.

Statistical analysis

All experiments were performed for a minimum of three biological replicates. When data points were pooled over multiple biological replicates, such as turnover, blebbing, or cortical enrichment data sets, data were plotted as Tukey plots, depicted with boxes (with median, Q1, Q3 percentiles), whiskers (minimum and maximum values within 1.5 times interquartile range), and outliers (solid circles). Statistical significance was assessed using the Mann–Whitney

U test in GraphPad Prism. For comparing data which were averaged for each biological replicate, such as comparison of pRLC or ppRLC levels, graphs showing the paired means (solid circles connected with lines) were created using GraphPad Prism. Statistical significance was determined using paired Student's *t* test in GraphPad Prism. Experiments where the means of each biological replicate were compared (Figure 4G), data was displayed as bar graphs and with error bars representing standard error of the means. For graphs displaying percentages, data from at least three biological replicates were pooled and no error bars were displayed.

ACKNOWLEDGMENTS

This work was funded by a MIRA from NIGMS (R35 GM125028) to D.T.B. and an American Heart Association Predoctoral Fellowship (18PRE33960551) to N.T.

REFERENCES

Barr FA, Gruneberg U (2007). Cytokinesis: Placing and Making the Final Cut. Cell 131, 847–860.

Beach JR, Bruun KS, Shao L, Li D, Swider Z, Remmert K, Zhang Y, Conti MA, Adelstein RS, Rusan NM, *et al.* (2017). Actin dynamics and competition for myosin monomer govern the sequential amplification of myosin filaments. Nat Cell Biol 19, 85–93.

Beach JR, Licate LS, Crish JF, Egelhoff TT (2011). Analysis of the role of Ser1/Ser2/Thr9 phosphorylation on myosin II assembly and function in live cells. BMC Cell Biol 12, 52.

Bennabi I, Crozet F, Nikalayevich E, Chaigne A, Letort G, Manil-Segalen M, Campillo C, Cadart C, Othmani A, Attia R, *et al.* (2020). Artificially decreasing cortical tension generates aneuploidy in mouse oocytes. Nat Commun 11, 1649.

Bergert M, Chandradoss SD, Desai RA, Paluch E (2012). Cell mechanics control rapid transitions between blebs and lamellipodia during migration. Proc Natl Acad Sci 109, 14434–14439.

Bovellan M, Romeo Y, Biro M, Boden A, Chugh P, Yonis A, Veghela M, Fritzsche M, Moulding D, Thorogate R, *et al.* (2014). Cellular control of cortical actin nucleation. Curr Biol 24, 1628–1635.

Chalut KJ, Paluch EK (2016). The Actin Cortex: A Bridge between Cell Shape and Function. Dev Cell 38, 571–573.

Charras G, Paluch E (2008). Blebs lead the way: how to migrate without lamellipodia. Nat Rev Mol Cell Biol 9, 730–736.

Charras GT, Coughlin M, Mitchison TJ, Mahadevan L (2008). Life and times of a cellular bleb. Biophys J 94, 1836–1853.

Charras GT, Hu C-K, Coughlin M, Mitchison TJ (2006). Reassembly of contractile actin cortex in cell blebs. J Cell Biol 175, 477–490.

Chew TG, Huang J, Palani S, Sommese R, Kamnev A, Hatano T, Gu Y, Oliferenko S, Sivaramakrishnan S, Balasubramanian MK (2017). Actin turnover maintains actin filament homeostasis during cytokinetic ring contraction. J Cell Biol 216, 2657–2667.

Chircop M (2014). Rho GTPases as regulators of mitosis and cytokinesis in mammalian cells. Small GTPases 5.

Chugh P, Clark AG, Smith MB, Cassani DAD, Dierkes K, Ragab A, Roux PP, Charras G, Salbreux G, Paluch EK (2017). Actin cortex architecture regulates cell surface tension. Nat Cell Biol 19, 689–697.

Chugh P, Paluch EK (2018). The actin cortex at a glance. J Cell Sci 131, jcs186254.

Connell LE, Helfman DM (2006). Myosin light chain kinase plays a role in the regulation of epithelial cell survival. J Cell Sci 119, 2269–2281.

Dean SO, Rogers SL, Stuurman N, Vale RD, Spudich JA (2005). Distinct pathways control recruitment and maintenance of myosin II at the cleavage furrow during cytokinesis. Proc Natl Acad Sci USA 102, 13473–13478.

Dulyaninova NG, Bresnick AR (2004). The long myosin light chain kinase is differentially phosphorylated during interphase and mitosis. Exp Cell Res 299, 303–314.

Dulyaninova NG, Patskovsky YV, Bresnick AR (2004). The N-terminus of the long MLCK induces a disruption in normal spindle morphology and metaphase arrest. J Cell Sci 117, 1481 LP–1493.

Fishkind DJ, Cao LG, Wang YL (1991). Microinjection of the catalytic fragment of myosin light chain kinase into dividing cells: effects on mitosis and cytokinesis. J Cell Biol 114, 967–975.

Fritzsche M, Erlenkämper C, Moeendarbary E, Charras G, Kruse K (2016). Actin kinetics shapes cortical network structure and mechanics. Sci Adv 2, e1501337.

Fujiwara K, Pollard TD (1976). Fluorescent antibody localization of myosin in the cytoplasm, cleavage furrow, and mitotic spindle of human cells. J Cell Biol 71, 848–875.

Guha M, Zhou M, Wang Y (2005). Cortical Actin Turnover during Cytokinesis Requires Myosin II. Curr Biol 15, 732–736.

Hickson GRX, Echard A, O'Farrell PH (2006). Rho-kinase controls cell shape changes during cytokinesis. Curr Biol 16, 359–370.

Ikebe M, Hartshorne DJ (1985). Phosphorylation of smooth muscle myosin at two distinct sites by myosin light chain kinase. J Biol Chem 260, 10027–10031.

Kassianidou E, Hughes JH, Kumar S (2017). Activation of ROCK and MLCK tunes regional stress fiber formation and mechanics via preferential myosin light chain phosphorylation. Mol Biol Cell 28, 3832–3843.

Kasza KE, Farrell DL, Zallen JA (2014). Spatiotemporal control of epithelial remodeling by regulated myosin phosphorylation. Proc Natl Acad Sci USA 111, 11732–11737.

Katoh K, Kano Y, Amano M, Kaibuchi K, Fujiwara K (2001). Stress fiber organization regulated by MLCK and Rho-kinase in cultured human fibroblasts. Am J Physiol Physiol 280, C1669–C1679.

Kondo T, Isoda R, Ookusa T, Kamijo K, Hamao K, Hosoya H (2013). Aurora B but not Rho/MLCK signaling is required for localization of diphosphorylated myosin ii regulatory light chain to the midzone in cytokinesis. PLoS One 8, e70965.

Kosako H, Yoshida T, Matsumura F, Ishizaki T, Narumiya S, Inagaki M (2000). Rho-kinase/ROCK is involved in cytokinesis through the phosphorylation of myosin light chain and not ezrin/radixin/moesin proteins at the cleavage furrow. Oncogene 19, 6059–6064.

Lancaster OM, Le Berre M, Dimitracopoulos A, Bonazzi D, Zlotek-Zlotkiewicz E, Picone R, Duke T, Piel M, Baum B (2013). Mitotic rounding alters cell geometry to ensure efficient bipolar spindle formation. Dev Cell 25, 270–283.

Levayer R, Lecuit T (2012). Biomechanical regulation of contractility: spatial control and dynamics. Trends Cell Biol 22, 61–81.

Liu H, Naismith JH (2008). An efficient one-step site-directed deletion, insertion, single and multiple-site plasmid mutagenesis protocol. BMC Biotechnol 8, 91.

Maddox AS, Lewellyn L, Desai A, Oegema K (2007). Anillin and the septins promote asymmetric ingression of the cytokinetic furrow. Dev Cell 12, 827–835.

Matsumura F, Yamakita Y, Yamashiro S (2011). Myosin light chain kinases and phosphatase in mitosis and cytokinesis. Arch Biochem Biophys 510, 76–82.

Mizutani T, Haga H, Koyama Y, Takahashi M, Kawabata K (2006). Diphosphorylation of the myosin regulatory light chain enhances the tension acting on stress fibers in fibroblasts. J Cell Physiol 209, 726–731.

Murthy K, Wadsworth P (2005). Myosin-II-Dependent Localization and Dynamics of F-Actin during Cytokinesis. Curr Biol 15, 724–731.

Paluch E, Piel M, Prost J, Bornens M, Sykes C (2005). Cortical actomyosin breakage triggers shape oscillations in cells and cell fragments. Biophys J 89, 724–733.

Ramanathan SP, Helenius J, Stewart MP, Cattin CJ, Hyman AA, Muller DJ (2015). Cdk1-dependent mitotic enrichment of cortical myosin II promotes cell rounding against confinement. Nat Cell Biol 17, 148–159.

Rapsomaniki MA, Cinquemani E, Giakoumakis NN, Kotsantis P, Lygeros J, Lygerou Z (2015). Inference of protein kinetics by stochastic modeling and simulation of fluorescence recovery after photobleaching experiments. Bioinformatics 31, 355–362.

Salbreux G, Charras G, Paluch E (2012). Actin cortex mechanics and cellular morphogenesis. Trends Cell Biol 22, 536–545.

Sedzinski J, Biro M, Oswald A, Tinevez J-Y, Salbreux G, Paluch E (2011). Polar actomyosin contractility destabilizes the position of the cytokinetic furrow. Nature 476, 462–466.

Sellers JR, Eisenberg E, Adelstein RS (1982). The binding of smooth muscle heavy meromyosin to actin in the presence of ATP. Effect of phosphorylation. J Biol Chem 257, 13880–13883.

Somlyo AV, Wang H, Choudhury N, Khromov AS, Majesky M, Owens GK, Somlyo AP (2004). Myosin light chain kinase knockout. J Muscle Res Cell Motil 25, 241–242.

Srivastava V, Robinson DN (2015). Mechanical stress and network structure drive protein dynamics during cytokinesis. Curr Biol 25, 663–670.

Taneja N, Bersi MR, Baillargeon SM, Fenix AM, Cooper JA, Ohi R, Gama V, Merryman WD, Burnette DT (2020). Precise tuning of cortical contractility regulates cell shape during cytokinesis. Cell Rep 31, 107477.

Taneja N, Burnette DT (2019). Myosin IIA drives membrane bleb retraction. Mol Biol Cell 30, 1051–1059.

Tinevez J-Y, Schulze U, Salbreux G, Roensch J, Joanny J-F, Paluch E (2009). Role of cortical tension in bleb growth. Proc Natl Acad Sci 106, 18581–18586.

Totsukawa G, Wu Y, Sasaki Y, Hartshorne DJ, Yamakita Y, Yamashiro S, Matsumura F (2004). Distinct roles of MLCK and ROCK in the regulation of membrane protrusions and focal adhesion dynamics during cell migration of fibroblasts. J Cell Biol 164, 427–439.

Toyoda Y, Cattin CJ, Stewart MP, Poser I, Theis M, Kurzchalia TV, Buchholz F, Hyman AA, Müller DJ (2017). Genome-scale single-cell mechanical phenotyping reveals disease-related genes involved in mitotic rounding. Nat Commun 8, 1266.

Uehara R, Hosoya H, Mabuchi I (2008). In vivo phosphorylation of regulatory light chain of myosin II in sea urchin eggs and its role in controlling myosin localization and function during cytokinesis. Cell Motil Cytoskeleton 65, 100–115.

Vicente-Manzanares M, Ma X, Adelstein RS, Horwitz AR (2009). Non-muscle myosin II takes centre stage in cell adhesion and migration. Nat Rev Mol Cell Biol 10, 778.

Watanabe T, Hosoya H, Yonemura S (2007). Regulation of myosin II dynamics by phosphorylation and dephosphorylation of its light chain in epithelial cells. Mol Biol Cell 18, 605–616.

Weirich KL, Stam S, Munro E, Gardel ML (2021). Actin bundle architecture and mechanics regulate myosin II force generation. Biophys J 120, 1957–1970.

Wu Q, Sahasrabudhe RM, Luo LZ, Lewis DW, Gollin SM, Saunders WS (2010). Deficiency in myosin light-chain phosphorylation causes cytokinesis failure and multipolarity in cancer cells. Oncogene 29, 4183–4193.

Yoshizaki H, Ohba Y, Parrini M-C, Dulyaninova NG, Bresnick AR, Mochizuki N, Matsuda M (2004). Cell type-specific regulation of RhoA activity during cytokinesis. J Biol Chem 120, 1957–1970.